

Hypersolid: Emergent Vision Representations via Short-Range Repulsion

Esteban Rodríguez-Betancourt¹ Edgar Casasola-Murillo²

Abstract

A recurring challenge in self-supervised learning is preventing representation collapse. Existing solutions typically rely on global regularization, such as maximizing distances, decorrelating dimensions or enforcing certain distributions. We instead reinterpret representation learning as a discrete packing problem, where preserving information simplifies to maintaining injectivity. We operationalize this in Hypersolid, a method using short-range hard-ball repulsion to prevent local collisions. This constraint results in a high-separation geometric regime that preserves augmentation diversity, excelling on fine-grained and low-resolution classification tasks.

1. Introduction

Most self-supervised learning methods optimize two complementary components: an *alignment* objective enforcing consistency across views, and a *separation* mechanism preventing collapse. While there is consensus on alignment, separation strategies differ substantially, with methods such as global expansion, redundancy reduction or specific output distributions.

Instead of tackling differential entropy maximization, we reframe representation learning as a discrete packing problem. We observe that for deterministic encoders, discrete Shannon entropy is bounded by input information; thus, preserving information simplifies to maintaining injectivity. We operationalize this in *Hypersolid*, a method treating embeddings as “hard balls” with a short-range exclusion zone. By enforcing local separability rather than global repulsion, we achieve an implicit discretization that is sufficient to prevent collapse. When paired with alignment, this simple geometric constraint leads to emergent, wider inter-class separation while preserving intra-class diversity,

¹Posgrado en Computación e Informática, Universidad de Costa Rica, San José, Costa Rica ²Escuela de Ciencias de la Computación e Informática, Universidad de Costa Rica, San José, Costa Rica. Correspondence to: Esteban Rodríguez-Betancourt <esteban.rodriguezbetancourt@ucr.ac.cr>.

Preprint. January 30, 2026.

resulting in high performance particularly on fine-grained and low-resolution classification tasks.

2. Related Work

Contrastive Learning and Global Expansion. Methods like SimCLR (Chen et al., 2020) and MoCo (He et al., 2020) enforce global repulsion, treating every image as a distinct class and pushing all negative pairs apart, aiming to expand the representation distribution to fill the latent space. In contrast, Hypersolid enforces a universal exclusion zone for all pairs. While positive pairs are aligned, they are strictly repelled if they breach this short-range radius, ensuring that even semantically identical views respect a minimum separation distance.

Non Contrastive Information Maximization. Barlow Twins (Zbontar et al., 2021) and VICReg (Bardes et al., 2022) minimize feature redundancy or enforce variance constraints, maximizing a proxy for differential entropy. Hypersolid does not optimize towards maximizing differential entropy; instead, it prevents information loss (in a discrete Shannon entropy sense) by pursuing almost-injectiveness in a probabilistic sense.

Clustering and Discretization. Clustering approaches like SwAV explicitly discretize the space via prototypes. Hypersolid shares a similar intuition regarding discretization but, rather than collapsing samples into shared prototypes, it attempts to distinguish every single augmentation.

Manifold Packing. CLAMP (Zhang et al., 2026) also models representations using short-range potentials. However, while CLAMP relies on statistical physics and submanifold measurements, Hypersolid is justified by a simpler entropy preservation entropy via injectivity.

Characterizations of the latent manifold. Wang & Isola (2020) identified uniformity and alignment as key geometric properties of high-quality representations. In this work, we demonstrate empirically that local collision avoidance combined with alignment is sufficient to induce isotropic, low-correlation distributions. However, we argue that uniformity alone is insufficient to capture the efficiency of the representation. We propose that high-quality manifolds should also be characterized by their intrinsic separability and topological efficiency, properties we quantify analytically via

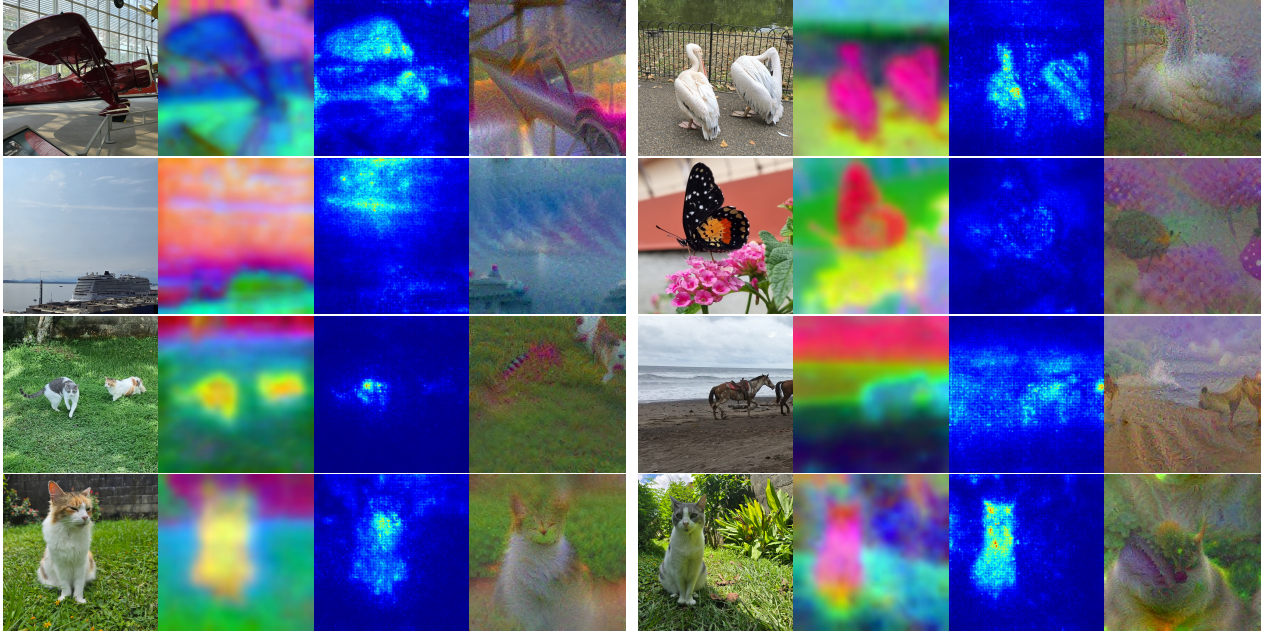


Figure 1. Hypersolid Qualitative Feature Analysis (ResNet-50 on ImageNet-1k). Left to Right: Input image, hypercolumn PCA, multi-layer Grad-CAM, and gradient-based feature inversion. Note the emergent semantic segmentation (warm colors on foregrounds), the foreground-oriented focusing bias, and the retention of fine-grained compositional details.

the Sensitivity Index (d') and our proposed Structure Ratio. This suggests that global uniformity is not necessarily a prerequisite objective, but instead an emergent effect of entropy preservation. Supporting this view, Slapik & Shouval (2026) provide biological evidence that complex cells facilitate object recognition through representational untangling, producing highly separable codes within low-dimensional subspaces. This aligns with our hypothesis that distinguishability is the minimal sufficient constraint for learning robust, information-preserving representations.

3. Method Description

Our method follows a structure similar to other self-supervised learning methods. We use a neural network to produce embeddings for different views of an image, then use those embeddings to build a target, and we train the network to follow those targets based on our loss function.

For producing the views, we opted to use the same recipe as DINO (Caron et al., 2021): at least two global views and N local views. Other than preserving a different size of the original image, global and local views are treated equally. The full list of augmentations is described in Section D.

Our loss function can be expressed as

$$\mathcal{L}_H = \mathcal{L}_{\text{alignment}} + \mathcal{L}_{\text{repulsion}} + \mathcal{L}_{\text{normalization}}$$

where $\mathcal{L}_{\text{alignment}}$ makes views have similar representation, $\mathcal{L}_{\text{repulsion}}$ strongly rejects representations that get too close,

and finally $\mathcal{L}_{\text{normalization}}$ applies a weak L_2 normalization, making the representations more easily separable using a linear probe. Full Torch source code of our loss function is included in the Section A.

3.1. Repulsion: Enforce Short Range Separation

We enforce a maximum cosine similarity α between all view embeddings (positive and negative). Crucially, gradients are zero for pairs with similarity below α . Formally, let $\mathcal{Z} = \{z_1, z_2, \dots, z_M\}$ be the set of all embeddings in the batch, where $M = B \times V$ (B images, each with V views). Then, the repulsion loss is expressed as:

$$\mathcal{L}_{\text{repulsion}} = \mathbb{E}_{z_i, z_j \in \mathcal{Z}} \left[\frac{\text{ReLU}(\cos(z_i, z_j) - \alpha)}{1 - \alpha} \right]$$

where the expectation is taken over all pairs in the batch.

This formulation represents a deliberate deviation from the standard objective of learning invariance under augmentation. By applying repulsion even to positive pairs (views of the same image), we enforce a minimum degree of separation between augmentations, effectively encouraging the model to maintain distinct, diverse features for each view rather than collapsing them to a single point.

The ReLU function creates a sparse gradient landscape, preventing the optimizer from wasting updates on separating representations that already satisfy the exclusion thresh-

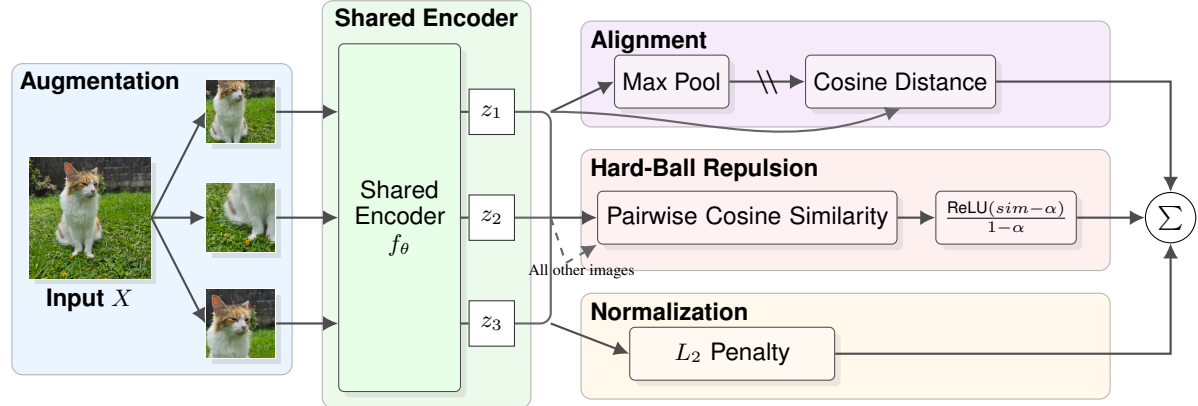


Figure 2. Hypersolid Training Workflow. An input image is augmented into global and local views and encoded. **Top (Purple):** Views are aligned to a “Feature Union” target created by max-pooling embeddings (with stop-gradient). **Middle (Red):** Short-range repulsion penalizes any pair (positive or negative) exceeding similarity α . **Bottom (Yellow):** A weak L_2 penalty regularizes feature magnitude.

old. Repulsion dominates only within the exclusion zone (similarity $> \alpha$), ensuring geometric constraints take precedence over alignment only when necessary.

3.2. Alignment: Feature Union via Max-Pooling

For the alignment term, we construct a target embedding for each source image by taking the dimension-wise maximum of the representations across its augmentations. Let $\mathcal{V} \subset \mathcal{Z}$ be the subset of embeddings corresponding to a single image. We define its target representation, z_{target} , as:

$$z_{\text{target}}^{(k)} = \max_{z \in \mathcal{V}} (z^{(k)})$$

where k indexes the feature dimension. This target acts as a bag of features, representing a union of all salient features visible across the augmentations. Empirically, we found that this max-pooling strategy prevented the early optimization stagnation observed when using a mean centroid.

Additionally, we apply a stop-gradient operation to the target. Without this, the optimization ends up reducing the magnitude of the view embeddings, rather than fully aligning them with the target, which causes early learning stagnation. The final alignment loss minimizes the cosine distance between each normalized view z_i and the normalized target z_{target} .

3.3. L_2 Embedding Normalization

Finally, we apply a weak penalty to the L_2 norm of the pre-normalized embeddings. Formally:

$$\mathcal{L}_{\text{normalization}} = \lambda (\mathbb{E}_z [\|z\|_2] - 1)^2$$

where the expectation is taken over all the views in the batch. This term serves two functions. First, it caps the growth of

feature magnitudes, ensuring that the max-pooling target selects features based on semantic activation rather than arbitrary scale. By preventing specific dimensions from dominating purely due to unbounded growth, this constraint actively mitigates representation anisotropy.

Second, the weight λ controls the optimization trajectory. We found that a weak penalty (such as $\lambda = 10^{-6}$) behaves better than a hard constraint. Unlike hard constraints that force geodesic updates, a weak penalty accelerates convergence by allowing the optimization to take shortcuts through the ambient space, while still capping the final representation scale.

4. Theoretical Justification

A direct consequence of the Data Processing Inequality is that for any deterministic encoder f , the output entropy is bounded by the input entropy: $\mathcal{H}(f(X)) \leq \mathcal{H}(X)$. Information cannot be created by a deterministic encoder, only preserved or discarded. Consequently, objectives that continue to expand feature volume after sufficient distinguishability is achieved may expend gradient capacity on objectives no longer aligned with information preservation.

In contrast, we interpret avoiding entropy collapse as a problem of collision avoidance in a discrete setting. For deterministic encoders, information loss occurs when f maps distinct inputs indistinguishable outputs. By minimizing $\mathcal{L}_{\text{repulsion}}$, we enforce that distinct samples occupy exclusive regions of radius $1 - \alpha$, which we interpret as a virtual discretization of the outputs. Once this geometric constraint is satisfied, the mapping becomes almost injective in a probabilistic sense, as there is no pair of embeddings mapping to the same discrete virtual symbol (region in the latent space).

Our repulsion loss is defined as

$$\mathcal{L}_{\text{repulsion}} = \mathbb{E} \left[\frac{\max(0, \cos(z_i, z_j) - \alpha)}{1 - \alpha} \right]$$

By Markov's inequality, we have

$$\mathbb{P}(\cos(z_i, z_j) > \alpha + \epsilon) \leq \frac{\mathcal{L}_{\text{repulsion}}(1 - \alpha)}{\epsilon},$$

where the probability is taken over pairs of representations obtained from the data distribution and augmentations. Therefore, the probability of collisions decreases as $\mathcal{L}_{\text{repulsion}} \rightarrow 0$, implying that the representation preserves input distinguishability with high probability, and entropy collapse due to collisions is avoided.

Therefore, Hypersolid prevents entropy collapse not by forcefully expanding the latent volume, but by preserving the distinguishability of the input samples. This allows the model to “rest” once the theoretical limit is reached, rather than fighting against the Data Processing Inequality.

Crucially, this goal does not compromise semantic clustering. In high-dimensional spaces, the kissing number grows exponentially, largely exceeding the cardinality of datasets like ImageNet by orders of magnitude. For instance, for $d = 512$, the kissing number lower bound presented by Fernández et al. (2025) is 2.46×10^{35} . Consequently, given enough model capacity, our constraint allows the model to pack thousands of semantically related variations tightly around a concept without exhausting the available geometric capacity.

5. Empirical Evaluation

5.1. Downstream Performance

Experimental Setup. We evaluate representations on STL-10 (Coates et al., 2011), CIFAR-10/CIFAR-100 (Krizhevsky & Hinton, 2009), and Food-101 (Bossard et al., 2014) using a ResNet-18 (200 epochs), and on ImageNet-1000 (Deng et al., 2009) using a ResNet-50 (100 epochs). We compare against a supervised baseline and six SSL methods: DINO (Caron et al., 2021), BYOL (Grill et al., 2020), Barlow Twins (Zbontar et al., 2021), SimCLR (Chen et al., 2020), VICReg (Bardes et al., 2022) and LeJEPA (Balestrieri & Le-Cun, 2025). To ensure rigorous reproducibility, we adopt the benchmarking setup of Kalapos & Gyires-Tóth (2024) and Lightly Framework of all SSL methods except for LeJEPA (we used their published code). All models were trained with AdamW ($LR = 10^{-3}$) in mixed precision on a single Nvidia H100 GPU, using a batch size of 512 for ImageNet-1k and 128 for all other datasets.

Results Analysis. Table 1 reports Top-1 accuracy for Linear Probe and k-NN classifiers ($K = 5$ for small-scale

Table 1. Linear probe and KNN accuracy

	METHOD	LINEAR		K-NN	
		TOP 1	TOP 5	TOP 1	TOP 5
STL-10	SimCLR	82.89	99.36	79.16	94.91
	BT	82.19	99.04	78.20	93.98
	HYPERSOLID	82.11	99.20	77.60	93.58
	VICREG	81.69	99.14	78.48	93.85
	BYOL	81.28	99.28	77.14	94.39
	LEJEPA	80.73	99.33	78.28	94.78
	DINO	79.75	99.11	76.85	93.53
CIFAR-10	SUPERVISED	71.86	97.41	72.43	87.69
	SUPERVISED	84.17	98.97	84.16	93.36
	HYPERSOLID	83.91	99.24	82.68	94.08
	LEJEPA	78.19	98.60	75.06	91.96
	VICREG	74.72	98.14	72.67	90.59
	BT	74.63	97.91	71.81	90.87
	SimCLR	72.58	97.86	69.16	90.25
CIFAR-100	DINO	72.46	98.02	70.07	90.34
	BYOL	69.37	97.81	65.54	89.74
	HYPERSOLID	55.06	82.44	51.92	70.27
	SUPERVISED	53.05	78.09	51.19	69.00
	LEJEPA	44.47	74.11	37.40	58.16
	VICREG	43.31	72.38	37.55	57.61
	BT	41.52	71.20	36.46	56.06
IM-1000	SimCLR	39.93	68.86	32.92	52.92
	DINO	39.27	68.42	34.07	53.06
	BYOL	38.68	68.84	33.91	53.72
	SUPERVISED	64.12	84.60	61.11	85.06
	HYPERSOLID	61.11	84.31	50.65	78.15
	DINO	58.49	82.42	49.72	78.06
	BT	57.51	81.06	45.03	73.20
Food-101	VICREG	57.47	80.81	45.26	73.23
	SimCLR	55.47	79.88	41.47	70.06
	BYOL	54.07	78.77	36.80	65.05
	LEJEPA	53.50	77.70	32.52	60.81
	SUPERVISED	71.33	89.59	70.01	90.35
	HYPERSOLID	71.32	90.57	64.27	86.57
	VICREG	65.69	87.34	56.61	81.19
	DINO	64.48	87.15	55.43	81.60
	BT	64.11	86.66	54.90	80.15
	LEJEPA	61.86	85.65	53.76	79.40
	SimCLR	61.15	85.07	49.99	77.45
	BYOL	58.21	82.75	45.83	73.85

datasets, $K = 200$ for ImageNet). On ImageNet-1k, Hypersolid exceeds the performance of the evaluated baselines. While results on STL-10 are comparable to other methods (within 0.78% of SimCLR), our method demonstrates improved accuracy on lower-resolution (CIFAR-10/100) and fine-grained (Food-101) benchmarks. The performance gap on Food-101 (+5.63% relative to VICReg) suggests that the packing objective may better preserve the high-frequency texture information often attenuated by standard invariance-based objectives. Complete training dynamics are detailed in Section F.

Table 2. Geometric Properties of Representations. We report metrics on ImageNet-1k (ResNet-50) and Food-101 (ResNet-18). Abbreviations: Aniso. (Anisotropy), Corr. (Feature Correlation), CVN (Center Vector Norm), SR (Structure Ratio), MPA (Mean Pairwise Angle), and d' (Sensitivity Index).

	METHOD	ANISO.	CORR.	CVN	CENTROID RANK	EMBED. RANK	SR	d'	SIGREG	MPA
IMAGENET-1000	SUPERVISED	0.29	0.043	0.53	651	1587	2.44	1.74	8.88	73.56°
	HYPERSOLID	0.11	0.036	0.33	535	1049	1.96	2.17	34.50	83.47°
	DINO	0.15	0.041	0.40	648	1521	2.35	1.83	28.90	80.97°
	LEJEPKA	0.47	0.041	0.72	413	1008	2.44	1.13	26.35	58.00°
	SIMCLR	0.66	0.056	0.82	426	1173	2.75	1.50	18.43	47.46°
	VICREG	0.73	0.043	0.86	468	1213	2.59	1.37	12.61	42.14°
	BARLOW TWINS	0.81	0.041	0.90	422	1138	2.69	1.31	13.71	35.10°
	BYOL	0.86	0.052	0.93	311	935	3.01	0.88	23.77	28.61°
Food-101	SUPERVISED	0.49	0.075	0.69	53	375	7.09	1.41	33.65	61.27°
	HYPERSOLID	0.19	0.074	0.48	69	315	4.59	1.92	124.13	76.51°
	BARLOW TWINS	0.21	0.077	0.48	64	365	5.69	1.27	36.90	76.45°
	DINO	0.28	0.064	0.54	56	394	7.01	1.23	50.31	72.77°
	VICREG	0.28	0.078	0.54	61	360	5.87	1.26	40.68	72.54°
	SIMCLR	0.41	0.087	0.65	46	332	7.27	1.05	41.97	64.57°
	LEJEPKA	0.61	0.067	0.81	40	299	7.39	0.93	42.67	48.83°
	BYOL	0.70	0.109	0.84	26	251	9.76	0.80	63.44	44.52°

5.2. Geometric Analysis

Manifold Uniformity and Capacity. Using our networks trained on ImageNet-1000 and Food-101, we measured several quantitative latent space properties, summarized in Table 2.

Surprisingly, even if our method focuses on local interactions, Hypersolid achieves low anisotropy, correlation and center vector norm (Jha et al., 2024), demonstrating it has learned well-distributed representations.

(Balestrieri & LeCun, 2025) identified that JEPAs’ embeddings should follow an isotropic Gaussian distribution to minimize downstream prediction risk. Under this metric (SIGReg), Hypersolid is a clear outlier, having the highest value within the evaluated methods. Hypersolid’s geometry is isotropic but not Gaussian, at least under the Euclidean assumption of SIGReg. This confirms that the geometry produced by Hypersolid is fundamentally different to the geometry produced by other models.

To describe further the geometry differences, we measured the effective rank (Roy & Vetterli, 2007) for the class centroids and the embeddings. Compared to other methods, Hypersolid seems to have a relatively high rank for class centroids, meaning that it uses more dimensions to “describe” them. On the other hand, Hypersolid seems to have a relatively lower rank for embeddings, suggesting that Hypersolid learns a low-rank representation of embeddings, while describing with high detail each class. This intuition was formalized into *Structure Ratio*, which we defined as $SR = \frac{\text{Embeddings Effective Rank}}{\text{Class Centroid Effective Rank}}$. This metric captures the relationship between global capacity of the embedding space

and the geometric complexity of the semantic categories. A lower ratio indicates that the model uses its available dimensionality to support the class topology in a more efficient way. Using this metric, Hypersolid achieves a much lower value (1.96 for ImageNet-100 and 4.59 for Food-101) than other methods. This aligns with recent findings in computational neuroscience (Slapik & Shouval, 2026), which suggest that the early visual system facilitates recognition specifically by compressing information into low-dimensional subspaces while maximizing representational untangling.

Pairwise Separability. To quantify the intrinsic safety of the representations against semantic hallucination, we employ the Sensitivity Index (d') from Signal Detection Theory (Roy & Vetterli, 2007). Unlike accuracy, which relies on a specific decision boundary, d' measures the statistical separation between the distribution of positive pair similarities (signal) and negative pair similarities (noise), normalized by their pooled variance. Hypersolid achieves a significantly higher sensitivity index than other SSL methods and even the supervised baseline.

Figure 3 presents a comprehensive comparison of pairwise cosine similarities across all evaluated methods. We observe two distinct geometric regimes. The first, occupied by Hypersolid, DINO and the supervised baseline, is characterized by a “high separation” profile: negative pairs are shifted to an exclusion zone near zero, while positive pairs exhibit high variance. Notably, Hypersolid displays the flattest positive distribution among these, suggesting better preservation of augmentation diversity. The second regime, including SimCLR, Barlow Twins, VICReg, LeJEPKA and

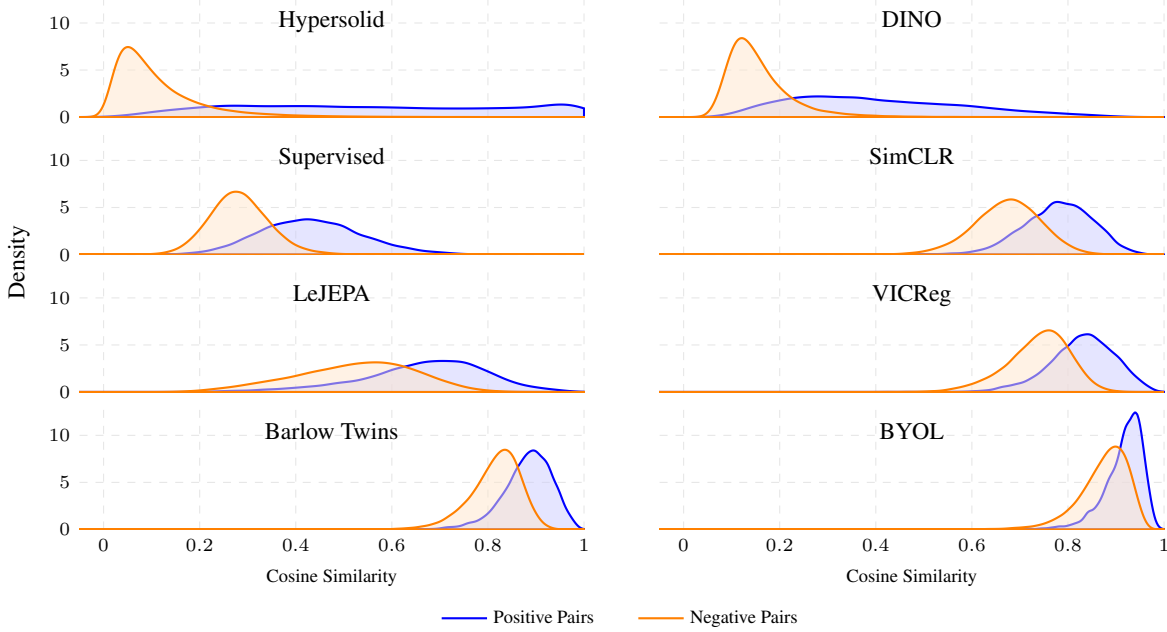


Figure 3. Pairwise Cosine Similarity Distributions (ImageNet-1000).

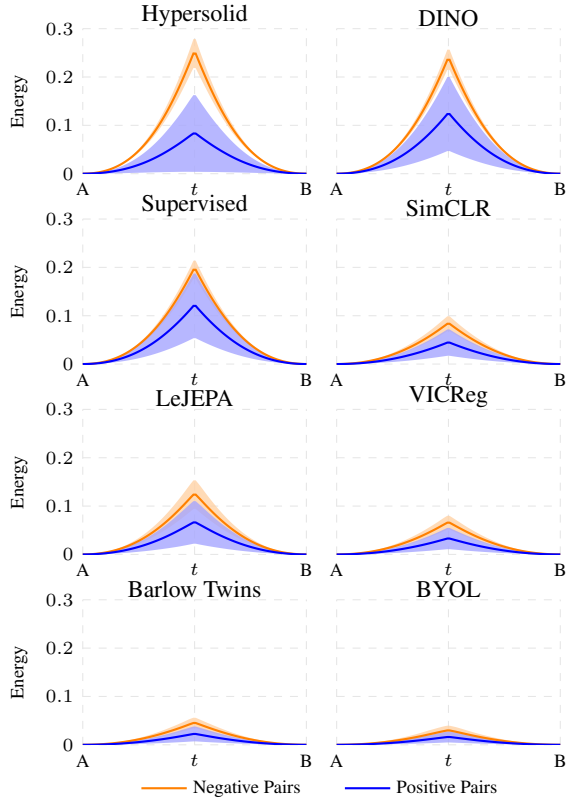


Figure 4. Semantic Topology Analysis on ImageNet-1000. Potential energy barriers for interpolation paths between random pairs, where solid lines represent the mean energy and shaded regions indicate ± 1 standard deviation across all pairs.

BYOL, is defined by “high overlap,” where positive and negative distributions share a significant support region in the high-similarity spectrum. This aligns with the sensitivity metric (d') reported in Table 2, where the first group consistently scores higher.

Both Hypersolid networks were trained using $\alpha = 0.9$, meaning the optimization just enforced a minimal angular distance of around 25.84° between pairs. Surprisingly, for Hypersolid the resulting geometry ended up with much bigger mean pairwise angles than other methods, with 83.47° in ImageNet-1000 and 76.51° in Food-101. This signals that, even if it may be counterintuitive, if we want bigger distances between all pairs, it is a better policy to just enforce a minimal distance and let the points self-organize.

Latent Energy Topology. To study the local geometry in Hypersolid, we performed interpolated walks between the ImageNet-1000 embeddings of randomly chosen pairs of images, and measured the energy potential of the interpolated points, measured as the cosine distance to the nearest true embedding. Our findings in Figure 4 show that Hypersolid topology has a wider gap between inter-class and intra-class walks. As distances between negative pairs are bigger, classifiers should be able to separate the identified clusters more easily. In addition, intra-class walks evidences a richer topology that varies from flat paths to slight elevations. This richer topology allows Hypersolid to express a more diverse set of internal similarities even within the same coarse group. This internal variability would explain the good results of Hypersolid in Food-101 dataset. On the

other hand, other methods exhibit a smaller gap between positive and negative pair walks. Interestingly, flatter paths are much less frequent in other methods than in Hypersolid. This suggests that the anti-collapse techniques used by other methods may be affecting their capacity of encoding similarity as smaller cosine distance.

Latent Energy Topology. To characterize the local geometry of Hypersolid, we performed linear interpolations between embeddings of randomly selected ImageNet-1000 image pairs. We defined the *energy potential* at each step as the cosine distance to the nearest neighbor in the validation set. As illustrated in Figure 4, Hypersolid exhibits a distinct topological regime characterized by a pronounced energy gap between inter-class (negative) and intra-class (positive) paths. The high energy barrier for negative pairs indicates a clean separation between class manifolds, creating a “void” that facilitates cluster discrimination. Conversely, intra-class trajectories reveal a rich topology characterized by low-energy “flat” paths, suggesting a dense and connected class structure. This connectivity allows Hypersolid to encode diverse internal similarities and semantic transitions within a coarse group, a capability that likely contributes to its better performance on fine-grained tasks like Food-101. In contrast, other methods exhibit significantly smaller energy gaps and fewer low-energy paths, suggesting that their anti-collapse mechanisms may inadvertently suppress the encoding of fine-grained semantic similarities by expanding the latent space too aggressively.

5.3. Qualitative Analysis

As shown in Figure 1, PCA projections of the hypercolumns reveal that Hypersolid learns emergent semantic segmentation. In multi-object images (e.g., pelicans, horses, cats), the model assigns similar spectral signatures to distinct instances, effectively isolating them from the background and identifying them as belonging to the same class. Notably, foreground objects predominantly map to warmer colors, suggesting the network utilizes high-variability components to encode salient features. This focus is corroborated by Grad-CAM maps of hypercolumns, which show gradient concentration biased towards foreground entities. Crucially, the feature inversions demonstrate retention of compositional structure and high-frequency details, such as the ring and head patterns of the cats. A comparison with DINO is provided in Section C and an explanation on how feature inversion was performed is provided in Section E.

6. Experiments

6.1. ImageNet-1000 and ResNet-50

We trained a ResNet-50 on ImageNet-1000 to compare the effects of mean vs max-pooling and effect of adding a weak

Table 3. Hyperparameter Sensitivity (CIFAR-100). Top-1 Linear and k-NN ($K = 5$) accuracy for a ResNet-18 trained for 200 epochs. Default settings are marked with *.

	VALUE	LINEAR ACC	KNN ACC
REF.	*ALL	55.06	51.92
	NEG. ONLY	43.46	43.42
	POS. ONLY	3.33	3.28
LR	1E-2	48.06	46.39
	*1E-3	55.06	51.92
	1E-4	50.73	48.04
ALPHA VALUE	0.10	52.24	46.09
	0.25	51.96	47.07
	0.50	53.64	50.07
	0.75	55.05	52.27
	0.85	55.88	52.81
	*0.90	55.06	51.92
	0.95	52.87	49.84
	0.975	49.21	43.89
BATCH SIZE	32	49.13	41.82
	64	52.94	50.51
	*128	55.06	51.92
	256	54.57	51.99
	512	53.97	51.08
	1024	51.95	48.50
	2048	48.77	45.20
PROJECTOR SIZE	64	54.19	51.23
	128	55.09	51.77
	256	54.72	51.75
	512	54.72	51.75
	*1024	55.06	51.92
	2048	55.65	53.27
	4096	55.96	52.02
LOCAL VIEWS	2	52.83	49.28
	4	54.95	50.89
	*6	55.06	51.92
	8	56.22	53.61
	10	55.50	52.90
	12	56.16	52.72
	14	56.38	53.56
	30	56.60	53.64

L_2 normalization. We used 10^{-3} for learning rate, 0.9 for α , 128 batch size, 1024 projector dimensions, 2 global views + 6 local views and a normalization weight of 10^{-6} .

Mean vs Max-pooling. We explored both options for building the alignment target and found mean-pooling to produce faster early learning, however, it quickly stagnates. On the other hand, max-pooling had indeed a slower start, but it continues improving without stagnating. As reference, with ResNet50 trained on ImageNet-1000 (both without L_2 normalization), we got a linear probe accuracy of 38.40% at the first epoch with mean pooling, while with max-pool we got just 25.52%. However, after epoch 10 max-pool surpasses mean-pool (mean had 47.77% accuracy and max-pool 47.80%). By epoch 48 mean pooling was just

at 49.47%, while max-pool version was at 54.78%.

L_2 normalization. We confirmed that a weak L_2 normalization can improve learning process. At a math level, this normalization prevents arbitrary magnitude increase, which was one concern after switching to max-pooling. On the other hand, it makes easier to linear probes to separate points, even if the angles themselves do not change. In ImageNet-1000 with a ResNet 50, disabling normalization ($\lambda = 0$) resulted in a final linear probe accuracy of 55.95%, while with a weak normalization of $\lambda = 10^{-6}$ achieved 61.11%. We expected this optimization to just help the linear probe, however, it also improved the KNN ($K = 200$) probe as well: without normalization the final accuracy was 47.59%, but with weak normalization the final accuracy at epoch 100 was 50.65%.

6.2. CIFAR-100 and ResNet-18

We trained a ResNet-18 for 200 epochs to isolate the effects of individual hyperparameters (default: LR = 10^{-3} , $\alpha = 0.9$, batch=128, projections=1024, 6 local views). Table 3 presents the full sweep results.

Repulsion. Applying repulsion to all pairs yielded the best performance. Restricting repulsion to negative-only pairs caused early instability and lower final accuracy (-11.6% linear probe), while positive-only repulsion failed completely.

Alpha value. We identified a “goldilocks” zone for the exclusion radius α between 0.75 and 0.90. Values outside this zone ended up with lower final accuracy.

Learning Rate. With AdamW optimizer, LR = 10^{-2} leads to faster early accuracy gains, followed by an early stagnation. A constant LR = 10^{-3} seems to work well. Smaller values such as LR = 10^{-4} are slower learners, but we do not observe learning stagnation.

Batch Size. We swept batch sizes (32-2048) on CIFAR-100. Performance peaked at 128; larger batches slowed learning, while smaller batches caused stalling. Regarding ViT architectures, preliminarily we found that ViT requires bigger batches, as mentioned in Section B.

Projector Size. Performance proved robust to projector width: scaling from 64 to 4096 dimensions yielded < 2% accuracy gain. We settled on 1024 as the optimal efficiency-performance trade-off.

Number of views. Increasing local views yields diminishing returns. While jumping from 2 to 4 views gains 2.1%, scaling further to 30 views adds only 1.6% despite the massive computational cost. We found 6 local views to be the optimal efficiency saturation point.

7. Limitations and Future Work

In this work, we prioritized verifying the fundamental geometric mechanism of discrete packing over large-scale architectural tuning. While our results on ViT-Tiny confirm that the objective generalizes to Transformer architectures and do not depend on convolutional inductive biases, we have not yet conducted the extensive hyperparameter exploration required to establish scaling laws for large-scale ViTs. Additionally, our current implementation utilizes a naive pairwise computation with $O((B \cdot V)^2)$ complexity. However, the short-range nature of the hard-ball potential inherently allows for efficient approximations (e.g., spatial hashing or neighbor lists), which we leave as a primary direction for future optimization.

8. Conclusions

In this work, we propose to reframe self-supervised learning as a “hard-ball packing” problem. It has theoretical advantages, such as being able to interpret mapping using discrete Shannon entropy, which can be maximized simply by achieving injectivity. We introduced Hypersolid, a method that operationalizes this insight through short range repulsion and feature-union alignment.

Our results demonstrate that this strategy is surprisingly effective: by replacing constant repulsion with a short range exclusion radius, Hypersolid allows the optimization to focus on semantic alignment, once enough distinctiveness is achieved. Our results show competitive accuracy in standard coarse-grained benchmarks like ImageNet-1k, and superior accuracy on fine-grained tasks or low resolution datasets, achieving +5.63% on Food-101 and +10.59% on CIFAR-100, compared to other evaluated methods.

Additionally, our geometric analysis proves that the resulting representations have properties fundamentally different to other methods, such as higher inter-class separation and a higher variance on intra-class separation.

We hope this work encourages a shift in perspective from maximizing manifold volume to maximizing symbolic packing, leveraging injectiveness and discrete Shannon entropy, allowing for more efficient and explainable representation learning methods in the future.

Impact Statement

This paper presents work whose goal is to advance the field of Machine Learning. There are many potential societal consequences of our work, none of which we feel must be specifically highlighted here.

References

Balestrieri, R. and LeCun, Y. LeJEPAP: Provable and scalable self-supervised learning without the heuristics, 2025. URL <https://arxiv.org/abs/2511.08544>.

Bardes, A., Ponce, J., and LeCun, Y. Vicreg: Variance-invariance-covariance regularization for self-supervised learning. In *ICLR*, 2022.

Bossard, L., Guillaumin, M., and Van Gool, L. Food-101 – mining discriminative components with random forests. In *European Conference on Computer Vision*, 2014.

Caron, M., Touvron, H., Misra, I., Jegou, H., Mairal, J., Bojanowski, P., and Joulin, A. Emerging properties in self-supervised vision transformers. In *2021 IEEE/CVF International Conference on Computer Vision (ICCV)*, pp. 9630–9640, 2021. doi: 10.1109/ICCV48922.2021.00951.

Chen, T., Kornblith, S., Norouzi, M., and Hinton, G. A simple framework for contrastive learning of visual representations. In *Proceedings of the 37th International Conference on Machine Learning*, ICML’20. JMLR.org, 2020.

Coates, A., Ng, A., and Lee, H. An analysis of single-layer networks in unsupervised feature learning. In Gordon, G., Dunson, D., and Dudík, M. (eds.), *Proceedings of the Fourteenth International Conference on Artificial Intelligence and Statistics*, volume 15 of *Proceedings of Machine Learning Research*, pp. 215–223, Fort Lauderdale, FL, USA, 11–13 Apr 2011. PMLR. URL <https://proceedings.mlr.press/v15/coates11a.html>.

Deng, J., Dong, W., Socher, R., Li, L.-J., Li, K., and Fei-Fei, L. Imagenet: A large-scale hierarchical image database. In *2009 IEEE Conference on Computer Vision and Pattern Recognition*, pp. 248–255, 2009. doi: 10.1109/CVPR.2009.5206848.

Dosovitskiy, A., Beyer, L., Kolesnikov, A., Weissenborn, D., Zhai, X., Unterthiner, T., Dehghani, M., Minderer, M., Heigold, G., Gelly, S., Uszkoreit, J., and Houlsby, N. An image is worth 16x16 words: Transformers for image recognition at scale. *ICLR*, 2021.

Fernández, I., Kim, J., Liu, H., and Pikhurko, O. New lower bounds on kissing numbers and spherical codes in high dimensions. *American Journal of Mathematics*, 147(4):901–925, August 2025. ISSN 0002-9327. doi: 10.1353/ajm.2025.a966288. Publisher Copyright: © 2025 by Johns Hopkins University Press.

Grill, J.-B., Strub, F., Altché, F., Tallec, C., Richemond, P., Buchatskaya, E., Doersch, C., Avila Pires, B., Guo, Z., Gheshlaghi Azar, M., et al. Bootstrap your own latent-a new approach to self-supervised learning. *Advances in neural information processing systems*, 33:21271–21284, 2020.

He, K., Fan, H., Wu, Y., Xie, S., and Girshick, R. Momentum contrast for unsupervised visual representation learning. In *2020 IEEE/CVF Conference on Computer Vision and Pattern Recognition (CVPR)*, pp. 9726–9735, 2020. doi: 10.1109/CVPR42600.2020.00975.

Jha, A., Blaschko, M. B., Asano, Y. M., and Tuytelaars, T. The common stability mechanism behind most self-supervised learning approaches. *arXiv*, 2024.

Kalapos, A. and Gyires-Tóth, B. Whitening consistently improves self-supervised learning. In *2024 International Conference on Machine Learning and Applications (ICMLA)*, pp. 448–453, 2024. doi: 10.1109/ICMLA61862.2024.00066.

Krizhevsky, A. and Hinton, G. Learning multiple layers of features from tiny images. Technical Report 0, University of Toronto, Toronto, Ontario, 2009. URL <https://www.cs.toronto.edu/~kriz/learning-features-2009-TR.pdf>.

Roy, O. and Vetterli, M. The effective rank: A measure of effective dimensionality. In *2007 15th European Signal Processing Conference*, pp. 606–610, 2007.

Slapik, M. B. and Shouval, H. Z. Simulated complex cells contribute to object recognition through representational untangling. *Neural Computation*, 38(2):145–164, 01 2026. ISSN 0899-7667. doi: 10.1162/NECO_a.1480. URL https://doi.org/10.1162/NECO_a.1480.

Wang, T. and Isola, P. Understanding contrastive representation learning through alignment and uniformity on the hypersphere. In *Proceedings of the 37th International Conference on Machine Learning*, ICML’20. JMLR.org, 2020.

Zbontar, J., Jing, L., Misra, I., LeCun, Y., and Deny, S. Barlow twins: Self-supervised learning via redundancy reduction. In Meila, M. and Zhang, T. (eds.), *Proceedings of the 38th International Conference on Machine Learning, ICML 2021, 18-24 July 2021, Virtual Event*, volume 139 of *Proceedings of Machine Learning Research*, pp. 12310–12320. PMLR, 2021. URL <https://proceedings.mlr.press/v139/zbontar21a.html>.

Zhang, G., Heeger, D. J., and Martiniani, S. Contrastive self-supervised learning as neural manifold packing, 2026. URL <https://arxiv.org/abs/2506.13717>.

A. PyTorch source code

The full code of our loss function is presented as follows:

```

1 class HypersolidLoss(nn.Module):
2     def __init__(self, alpha=0.9, norm_factor=1e-6):
3         super().__init__()
4         self.alpha = alpha
5         self.norm_factor = norm_factor
6
7     def forward(self, feats):
8         B, V, D = feats.shape
9         x = F.normalize(feats, dim=-1)                      # [B, V, D]
10
11    # Alignment term:
12    targets, _ = feats.max(dim=1, keepdim=True)    # [B, 1, D]
13    c = F.normalize(targets, dim=-1).detach()        # [B, 1, D]
14    pos_sim = x @ c.transpose(1, 2)                 # [B, V, 1]
15    pos_sim = pos_sim.squeeze(2)                   # [B, V]
16
17    alignment_loss = (1 - pos_sim).mean()
18
19    # Pairwise Repulsion term:
20    all_feats = x.reshape(B*V, D)                  # [B*V, D]
21    sim = all_feats @ all_feats.T                  # [B*V, B*V]
22    eye = torch.eye(B*V, dtype=torch.bool, device=x.device)
23    sim[eye] = 0.0                                # remove self-similarity
24
25    repulsion_loss = F.relu(sim - self.alpha) / (1 - self.alpha)
26    repulsion_loss = repulsion_loss.mean()
27
28    # Normalization term
29    norm_loss = (feats.norm(p=2, dim=-1).mean() - 1)**2
30    norm_loss = norm_loss * self.norm_factor
31
32    return alignment_loss + repulsion_loss + norm_loss

```

B. Preliminary Results on Vision Transformers

While our primary analysis focuses on ResNet architectures, we also evaluated the compatibility of our method with Vision Transformers. We trained a ViT-Tiny (patch size 16, image size 224) (Dosovitskiy et al., 2021) on STL-10 for 100 epochs with a batch size of 64. We maintained the same optimization configuration as our main results (AdamW, learning rate 10^{-3} , weight decay 10^{-6}). Using a batch size of 32 did not lead to any meaningful learning.

This model achieved a final linear probe top-1 accuracy of 72.29% and k-NN ($K = 5$) accuracy of 67.84%. Notably, we observed that ViT backbones require larger batch sizes to converge under our objective; training with a batch size of 32 resulted in learning stagnation (accuracy $< 5\%$). These preliminary results suggest that Hypersolid is not reliant on the inductive biases of convolutional networks. However, fully exploiting the capabilities of Vision Transformers likely requires a distinct hyperparameter exploration, which we did not attempt in this work. Despite this, qualitative analysis reveals a promising property: attention maps from the ViT-Tiny model exhibit distinct object-centric segmentation, often localizing objects effectively. As shown in Figure 5, the network attention often focus on the foreground object, even with out-of-distribution entities such as the butterfly (not part of STL-10). On the other hand, while the visualization of the PCA projection of the last layer is “blocky” (due to the low number of patches in ViT-Tiny), the foreground objects are still distinguishable with different colors from the background.

C. Visual Comparison with DINO

In Figure 1 we showed PCA projections, Grad-CAM visualization and images produced using feature inversion, using the features produced by a ResNet-50 trained using Hypersolid. To offer a point of comparison, Figure 6 presents the same visualizations for a ResNet-50 trained with DINO on ImageNet-1000 (our second-best performing method).

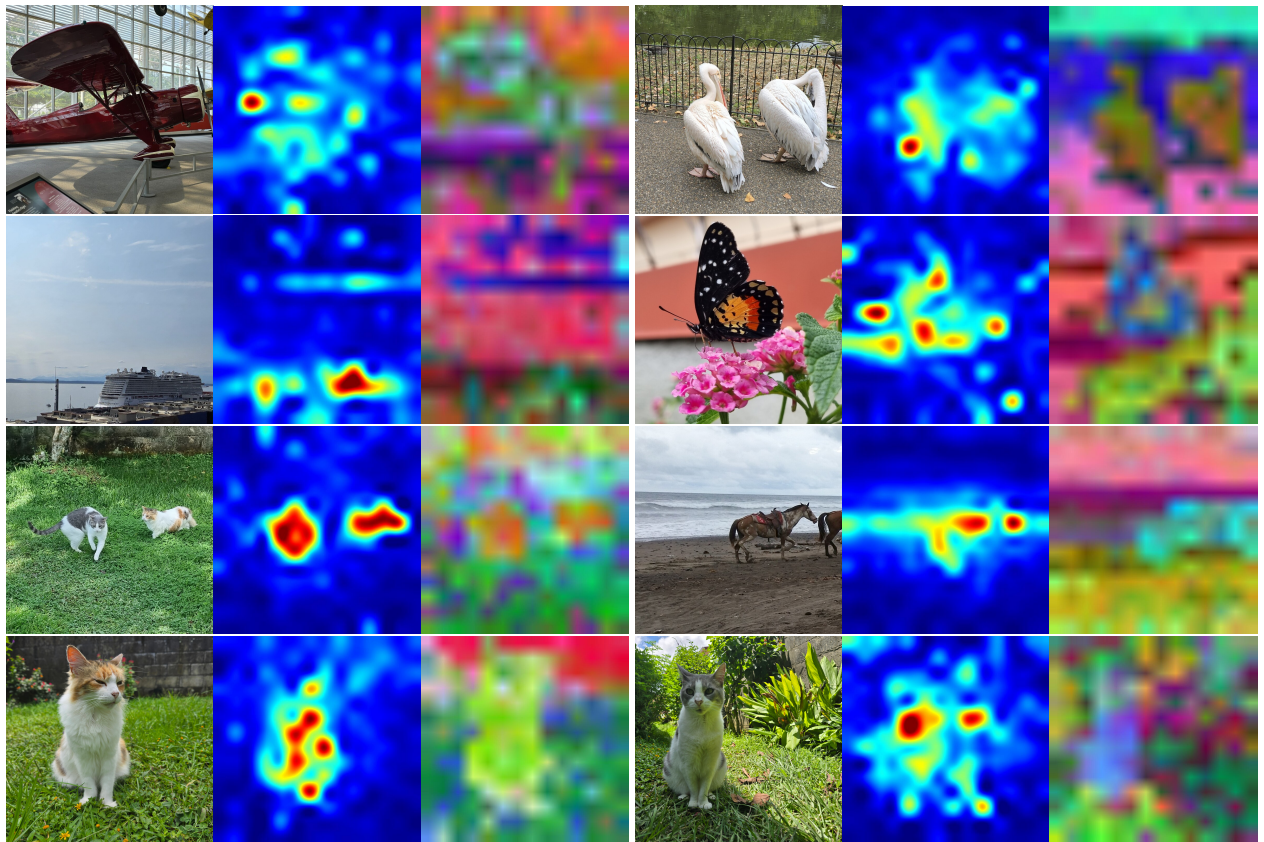


Figure 5. Qualitative analysis of a ViT-Tiny trained on STL-10. Despite the limited capacity, data regime (STL-10) and smaller batch size, the model attention still bias towards “foreground objects”. Due to lower resolution of the ViT-Tiny patch tokens the PCA projection is harder to appreciate. Still some semantic differentiation can be appreciated, such as the pelicans in brown, the two cats in orange or the horses in cyan.

Qualitative Differences. Comparing the PCA projections establishes that while both methods successfully isolate objects, they employ different feature subspaces, as evidenced by the distinct color palettes. A key divergence appears in the feature inversions: DINO produces “collage-like” reconstructions with higher realism but tends to hallucinate object repetition artifacts (note the boat in the sky and cats repetitions). In contrast, Hypersolid yields “painterly” reconstructions that appear to be more aligned with the original scene composition. This suggests that Hypersolid representations together with network knowledge may be encoding aspects such as object count or relative positioning. However, without formal measurements these observations remain qualitative.

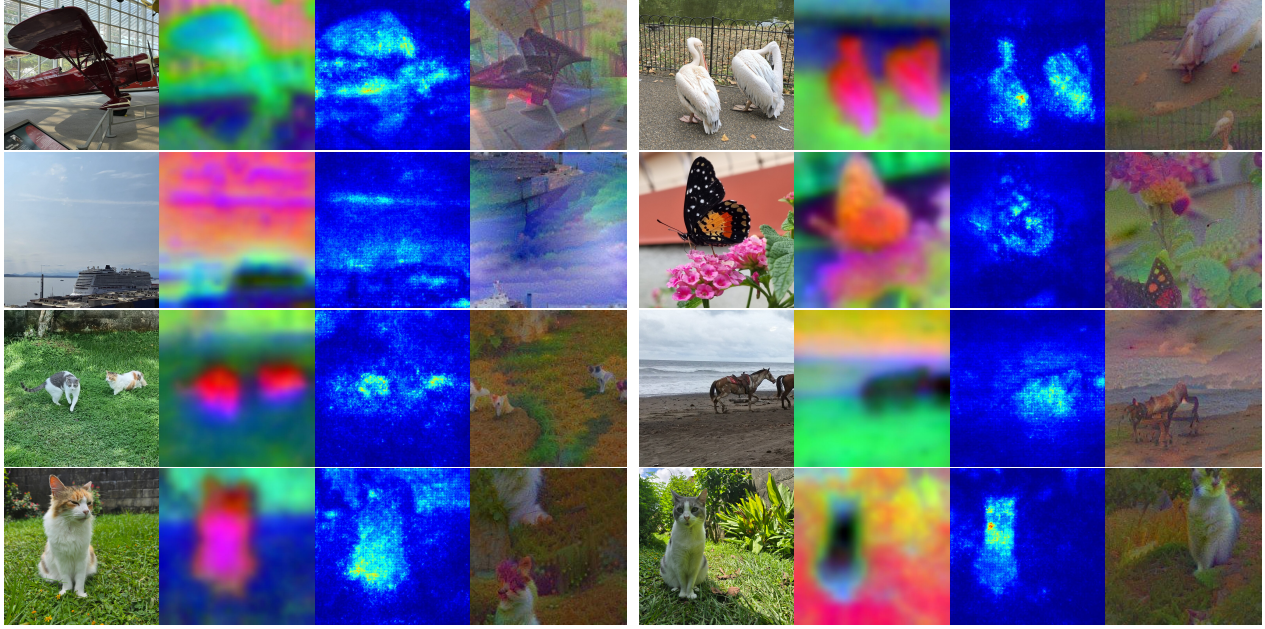


Figure 6. Visualization of learned features by DINO (ResNet-50 trained on ImageNet-1000). From left to right: PCA projection of hypercolumns, grad-cam visualization of all layers and an image produced using feature inversion.

D. Training Augmentations

For our augmentations pipeline, we leveraged the Lightly Framework `DINOTransform` class. The value of the parameters is described in Table 4. For ImageNet-1000 and Food-101, we used the default `DINOTransform` settings for both Hypersolid and DINO. The selected values were not fine-tuned, its choosing was based on dataset images size and network restrictions.

E. Feature Inversion

To visualize the information retained by the representations, in Figures 1 and 6 we employed a gradient-based feature inversion method. The objective was to synthesize an image \hat{x} such that its embedding $f(\hat{x})$ matches the target embedding $z_{\text{target}} = f(x)$ of a real image. We optimize the input pixels directly via backpropagation, while keeping the model weights frozen.

We opted to use a multi-scale optimization strategy. The process begins with a low resolution canvas (28×28 pixels) and progressively upsamples to the final resolution (224×224) across 5 scales (0.125, 0.25, 0.5, 0.75 and 1.0). At each transition, the canvas is upsampled using bicubic interpolation.

To generate the image, we minimized the following loss function:

$$\mathcal{L} = \mathcal{L}_{\text{content}} + \lambda \mathcal{L}_{\text{TV}}$$

where $\mathcal{L}_{\text{content}}$ minimizes the cosine distance between the current and target embeddings. And \mathcal{L}_{TV} suppresses high-frequency noise and checkerboard artifacts, enforcing spatial smoothness:

Table 4. Augmentations used in Hypersolid

PARAMETER	LIBRARY DEFAULT	CHANGES
GLOBAL CROP SIZE	224	CIFAR: 32, STL-10: 96
GLOBAL CROP SCALE	(0.4, 1.0)	CIFAR: (0.8, 1.0)
LOCAL CROP SIZE	96	CIFAR: 32, STL-10: 48, ViT: 224
LOCAL CROP SCALE	(0.05, 0.4)	CIFAR: (0.08, 0.9)
NUMBER OF LOCAL VIEWS	6	
HORIZONTAL FLIP PROB.	0.5	
VERTICAL FLIP PROB.	0	
RANDOM ROTATION PROB.	0	
RANDOM ROTATION DEGREES	NONE	
COLOR JITTER PROB.	0.8	
COLOR JITTER STRENGTH	0.5	
BRIGHTNESS JITTER	0.8	
CONTRAST JITTER	0.8	
SATURATION JITTER	0.4	
HUE JITTER	0.2	
RANDOM GRayscale PROB.	0.2	
GAUSSIAN BLUR	(1.0, 0.1, 0.5)	CIFAR: DISABLED
GAUSSIAN BLUR SIGMAS	(0.1, 2)	
KERNEL SIZE	NONE	
KERNEL SCALE	NONE	
SOLARIZATION PROB.	0.2	
NORMALIZATION	IMAGENET MEAN/STD	

$$\mathcal{L}_{TV} = \sum_{i,j} |x_{i+1,j} - x_{i,j}| + |x_{i,j+1} - x_{i,j}|$$

We used a weight $\lambda = 2$.

Finally, to improve further the resulting images, we applied the following regularization techniques during the optimization loop (Adam optimizer, $\eta = 0.05$, 4000 steps per scale):

1. Random Jitter: the input image is randomly shifted by up to ± 32 pixels before each forward pass to encourage translation invariance.
2. Periodic Gaussian Smoothing: Every 50 iterations, we apply a Gaussian blur ($\sigma = 0.5$, kernel size 5×5) to the canvas to prevent the accumulation of high-frequency noise.

F. Learning Dynamics and Training Curves

While Table 1 reports converged performance across datasets, the evolution accuracy during training can differ substantially between methods, particularly in early epochs. These dynamics are informative for understanding optimization behavior, stability and convergence speed, and we consider that may be useful for practitioners and researchers when assessing whether a training run is progressing as expected. For completeness, we report linear-probe and k-NN accuracy as a function of training epoch for STL-10 (Figures 7 and 8), CIFAR-10 (Figures 9 and 10), CIFAR-100 (Figures 11 and 12), ImageNet-1000 (Figures 13 and 14) and Food-101 (Figures 15 and 16).

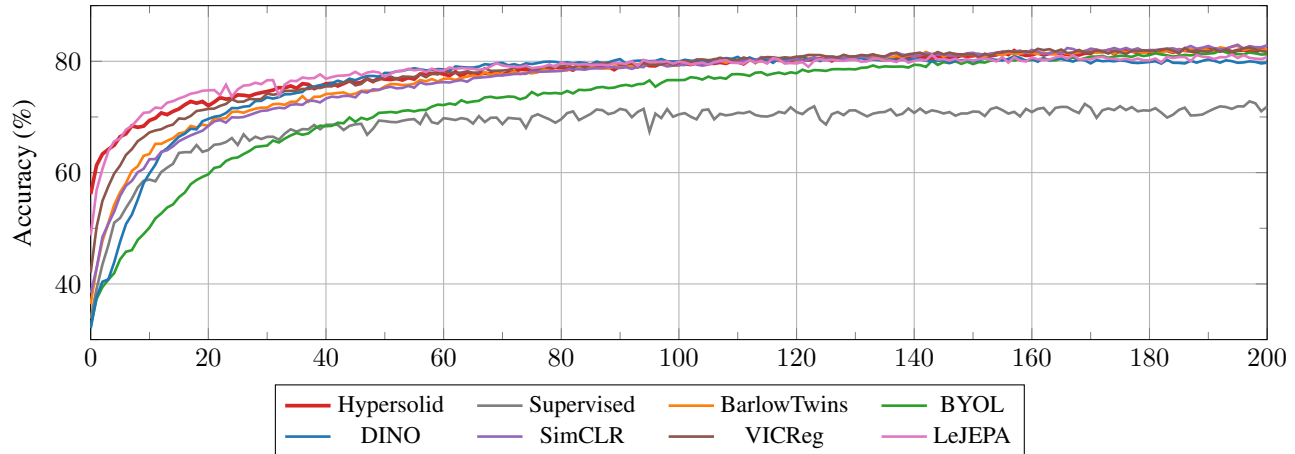


Figure 7. Linear probe top-1 accuracy on STL-10, per epoch

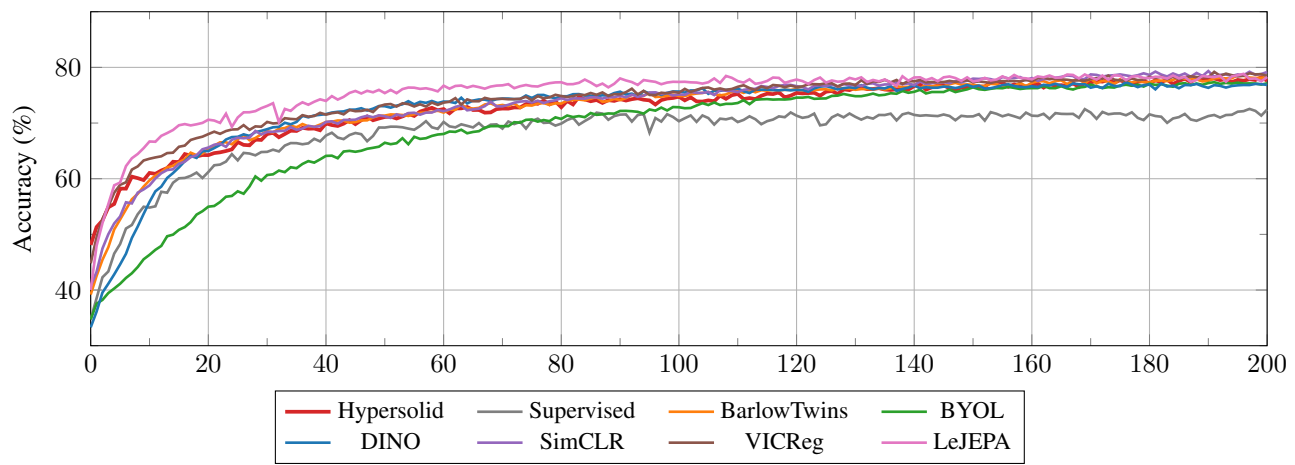


Figure 8. KNN classifier top-1 accuracy on STL-10, per epoch

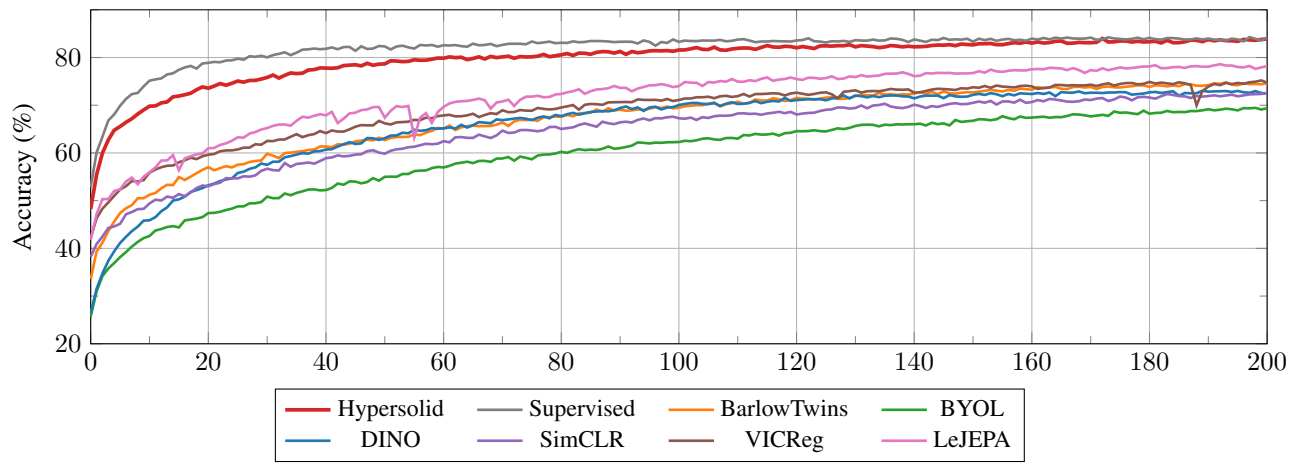


Figure 9. Linear probe top-1 accuracy on CIFAR-10, per epoch

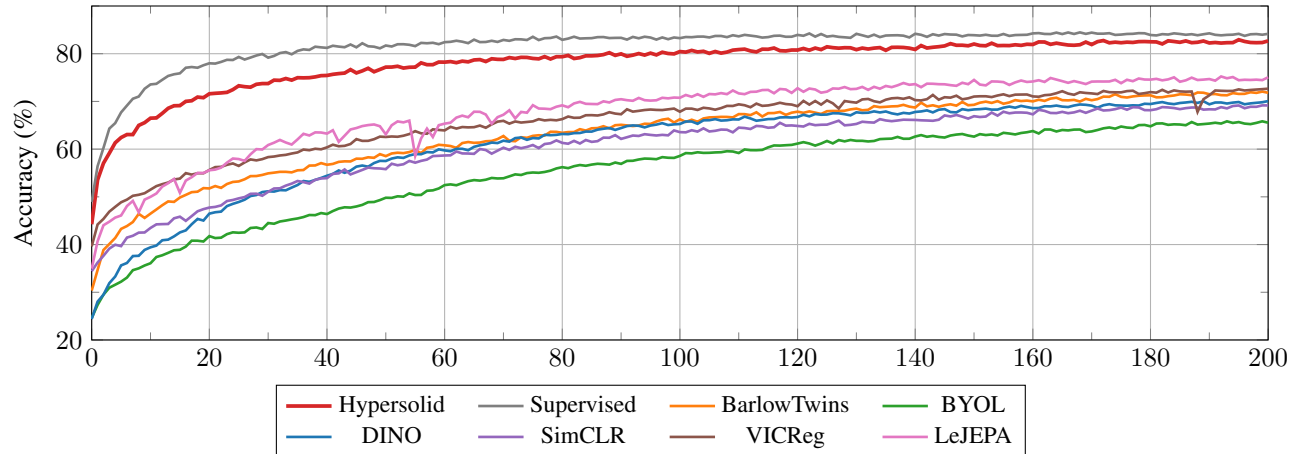


Figure 10. KNN classifier top-1 accuracy on CIFAR-10, per epoch

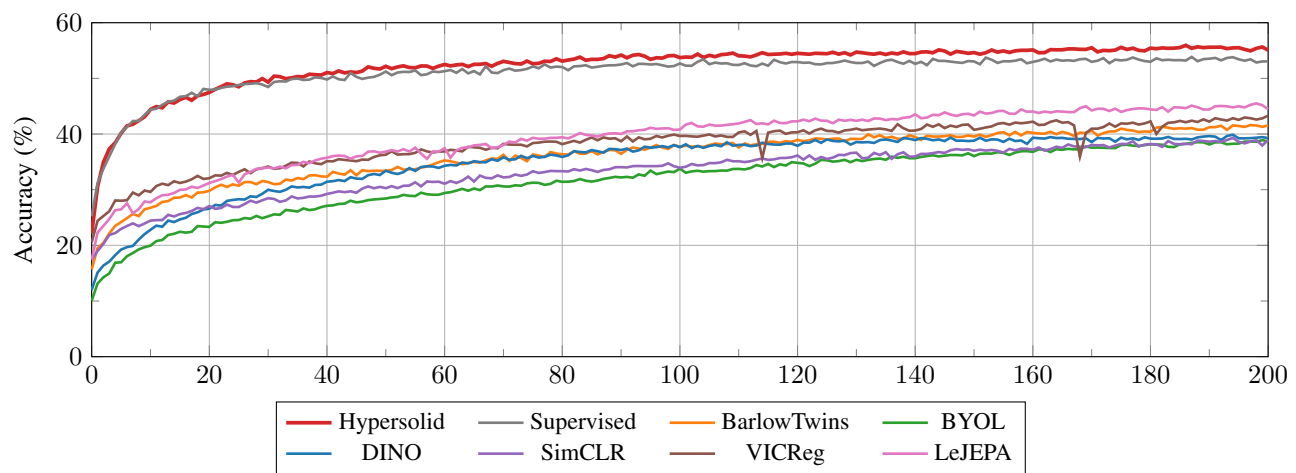


Figure 11. Linear probe top-1 accuracy on CIFAR-100, per epoch

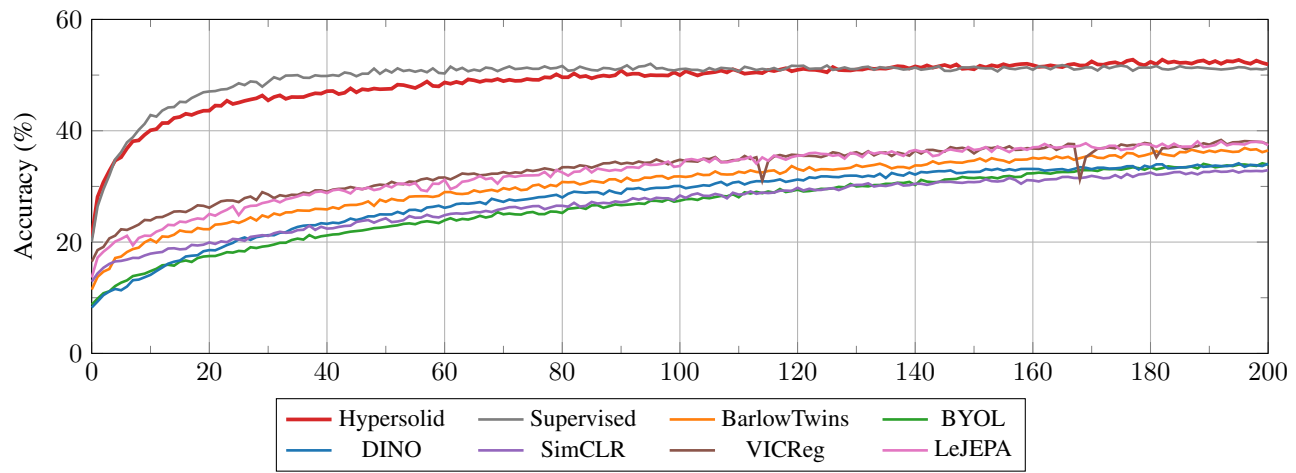


Figure 12. KNN classifier top-1 accuracy on CIFAR-100, per epoch

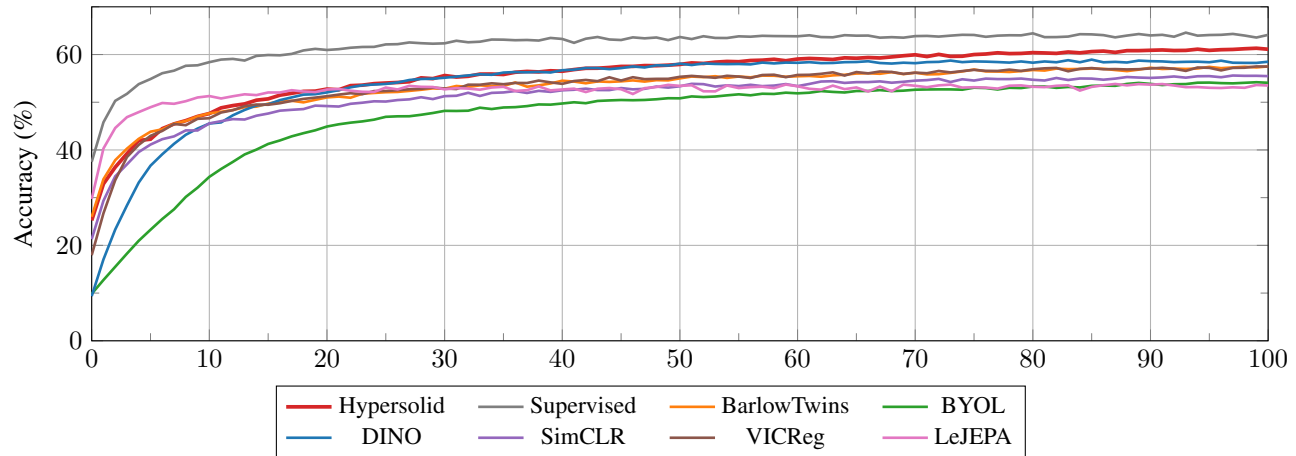


Figure 13. Linear probe top-1 accuracy on ImageNet-1k, per epoch

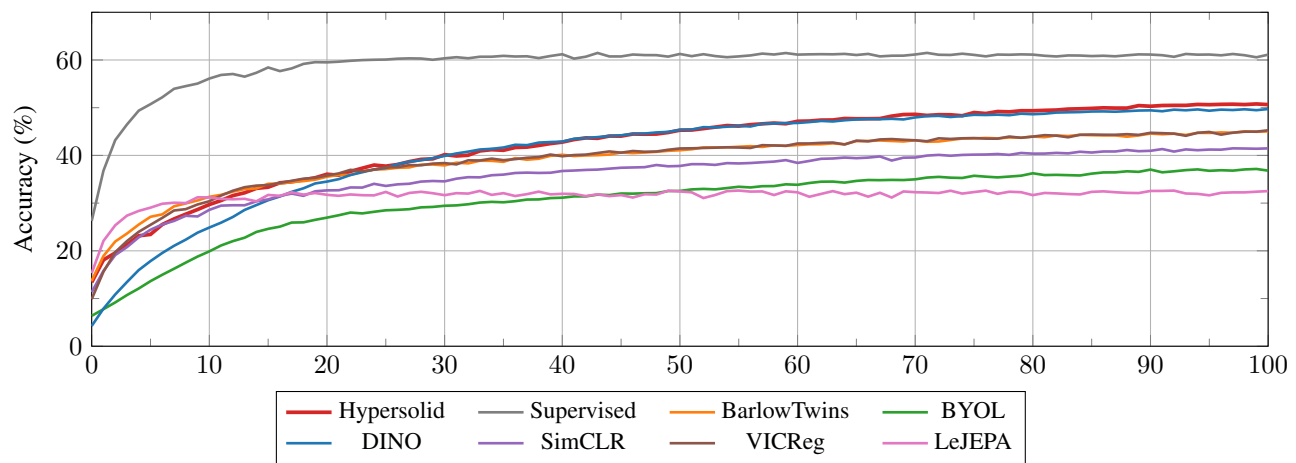


Figure 14. KNN classifier top-1 accuracy on ImageNet-1k, per epoch

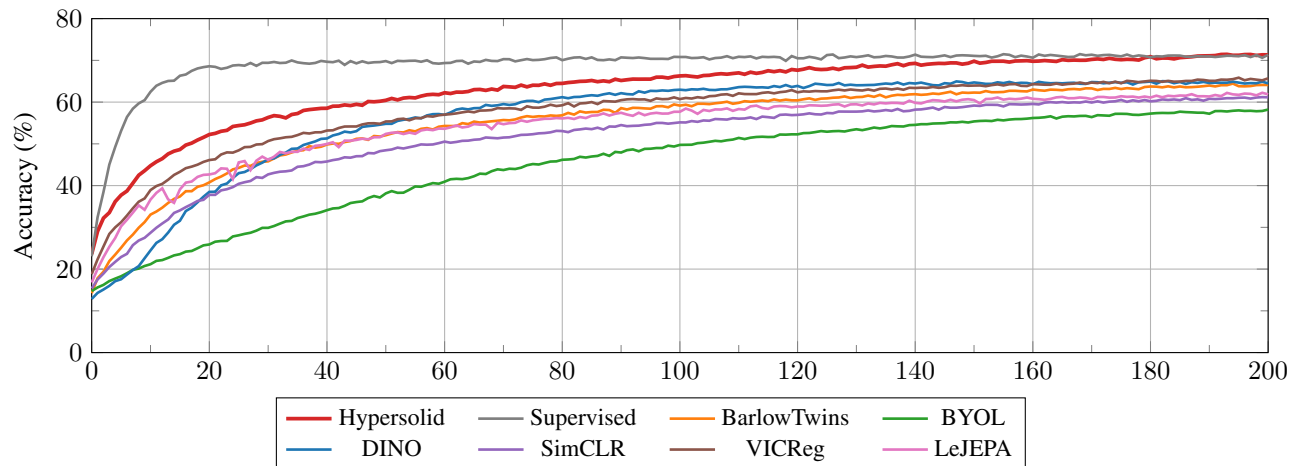


Figure 15. Linear probe top-1 accuracy on Food-101, per epoch

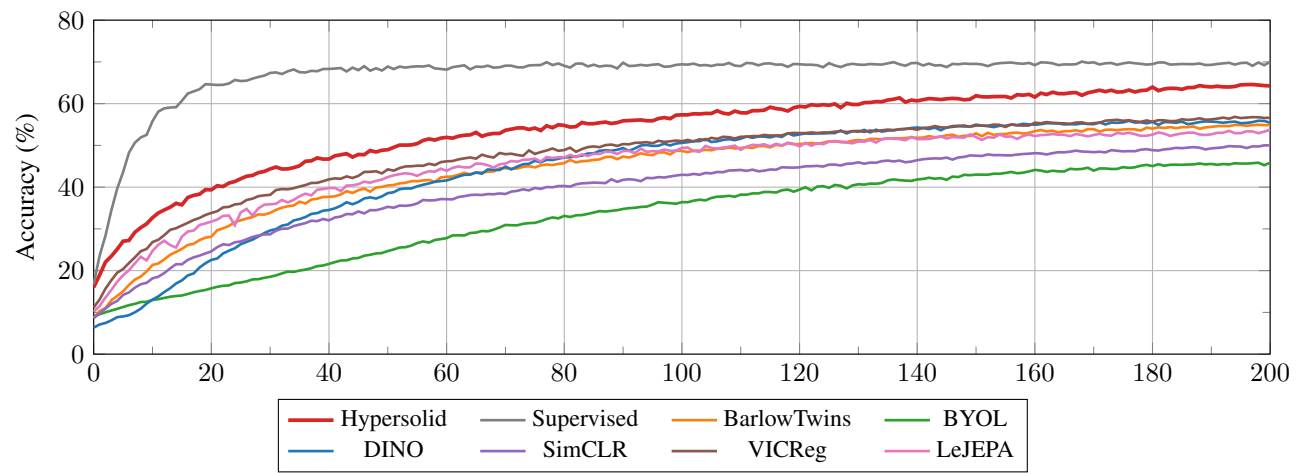


Figure 16. KNN classifier top-1 accuracy on Food-101, per epoch